COMPUTER METHODS IN APPLIED MECHANICS AND ENGINEERING 8 (1976) 249–276

A FINITE ELEMENT METHOD FOR A CLASS OF CONTACT-IMPACT PROBLEMS

Thomas J.R. HUGHES, Robert L. TAYLOR, Jerome L. SACKMAN,
Alain CURNIER and Worsak KANOKNUKULCHAI

Division of Structural Engineering and Structural Mechanics, Department of Civil Engineering
University of California, Berkeley, California 94720, U.S.A.

Received 17 September 1975

We present a finite element method for a class of contact-impact problems. Theoretical background and numerical implementation features are discussed. In particular, we consider the basic ideas of contact-impact, the assumptions which define the class of problems we deal with, spatial and temporal discretizations of the bodies involved, special problems concerning the contact of bodies of different dimensions, discrete impact and release conditions, and solution of the nonlinear algebraic problem. Several sample problems are presented which demonstrate the accuracy and versatility of the algorithm.

1. Introduction

In recent years large-scale computational capabilities have been developed in many areas of structural analysis. The primary technique used in these developments is the finite element method. At the same time, very few capabilities are available for complicated structural problems involving contact-impact effects, an area of considerable importance in science and technology. In fact, it appears that only small-deformation quasi-static problems have been considered thus far (see [1–3]). This is not surprising as contact-impact phenomena are inherently nonlinear and the resulting problems are difficult.

In this paper we summarize some aspects of our work in developing numerical algorithms for general contact-impact problems in continuum mechanics. In section 2 we discuss the basic concepts associated with contact-impact problems and develop the interface conditions for the simple cases of frictionless and perfect-friction contact. In section 3 we describe a class of contact-impact problems, termed "Hertzian" problems, in which simplifications of a geometric and kinematic nature are made which lead to a simple numerical formulation. Spatial discretization aspects of this formulation, involving finite element techniques, are discussed in section 4. In section 5 we consider how these notions extend to problems involving the contact of bodies of different dimensions (e.g. a three-dimensional solid and a two-dimensional plate).

The spatially discretized equations of motion – a system of ordinary differential equations – is temporally discretized using the Newmark algorithm. Basic features of this technique are summarized in section 6. A point that we wish to stress here is the great care required to obtain accurate numerical results for impact problems of a wave-propagation nature. In section 7 we outline some discrete schemes, based upon exact results of wave-propagation theory, which enable us to very accurately simulate the solution of impact problems involving discontinuous stress waves.

In section 8 we indicate how we solve the resulting nonlinear algebraic system of equations and summarize the main steps of the algorithm.

Finally, in section 9, we present the results of some numerical computations based upon the previous theory. The importance of the discrete impact and release conditions discussed in section 7 is clearly shown.

2. Basic ideas of contact-impact

It is usual for the term *contact* to have a static connotation whereas *impact* has a dynamic one. Here we use *contact* in the general sense to include static as well as dynamic phenomena.

We identify a *body* B with its initial configuration, and we assume B is an open region of R^3 with a piecewise smooth boundary ∂B. A *contact problem* is a boundary-value problem, or an initial-boundary-value problem in which two bodies B^1 and B^2 interact according to the principles of the mechanics of continuous media. Thus the primary kinematic axiom of a contact problem is that configurations b^1 and b^2 of B^1 and B^2, respectively, do not penetrate each other, i.e.

$$b^1 \cap b^2 = \emptyset \,. \tag{1}$$

We refer to (1) as the *impenetrability condition*.

On the other hand, the unique condition which characterizes contact problems is that material points on the boundaries of B^1 and B^2 may coalesce during the motion of the bodies. Thus we say B^1 and B^2 are in contact if $\partial b^1 \cap \partial b^2 \neq \emptyset$, and we define the *contact surface* c by

$$c = \partial b^1 \cap \partial b^2 \,. \tag{2}$$

If B^1 and B^2 are never in contact, then $c = \emptyset$ for all configurations b^1 and b^2, and in this case an initial-boundary-value problem for B^1 and B^2 reduces to one in which B^1 and B^2 may be treated separately. A non-trivial contact problem is one in which $c \neq \emptyset$ for at least one instant during the motion of B^1 and B^2. These notions are illustrated in fig. 1. Eq. (1) indicates that c is a material

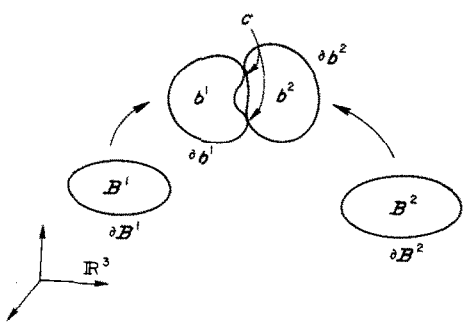

Fig. 1. Contacting bodies.

surface with respect to both bodies, i.e. one which is not crossed by material particles. From this we may deduce the interface conditions on c.

We say $\boldsymbol{x} \in c$ is a *persistent point* of c if joining or releasing of the bodies is not instantaneously occurring at $\boldsymbol{x}$. Let $\boldsymbol{x} \in c$ be persistent and denote by $\boldsymbol{v} = \dot{\boldsymbol{x}}$ its velocity. Note that only the normal part of $\boldsymbol{v}$ is independent of the parameterization of c. Let $\boldsymbol{v}^1$ and $\boldsymbol{v}^2$ be the velocities of the material particles located at the points $\boldsymbol{x}^1$ and $\boldsymbol{x}^2$ contained in ∂b^1 and ∂b^2, respectively, such that $\boldsymbol{x} = \boldsymbol{x}^1 = \boldsymbol{x}^2$ at the present instant. Then, since c is material and $\boldsymbol{x}$ is persistent,

$$\boldsymbol{v} \cdot \boldsymbol{n} = \boldsymbol{v}^1 \cdot \boldsymbol{n} = \boldsymbol{v}^2 \cdot \boldsymbol{n} , \tag{3}$$

where $\boldsymbol{n}$ is a unit normal vector to c at $\boldsymbol{x}$.

On the other hand, for momentum to be balanced at $\boldsymbol{x}$, it is required that

$$\boldsymbol{t}^1 + \boldsymbol{t}^2 = \boldsymbol{o} , \tag{4}$$

where $\boldsymbol{t}^\alpha$ is the Cauchy traction vector with respect to ∂b^α.

In addition we assume that no tensile tractions can occur on c:

$$\boldsymbol{t}^\alpha \cdot \boldsymbol{n}^\alpha \leqslant 0 , \tag{5}$$

where $\boldsymbol{n}^\alpha$ is the outward unit normal vector to ∂b^α. This condition precludes the possibility of two bodies becoming "glued" together. Conditions (1)–(5) characterize our notion of a contact problem.

More specific conditions on the tangential parts of $\boldsymbol{v}^\alpha$ and $\boldsymbol{t}^\alpha$ are determined by the frictional nature of the contact.

In the sequel we shall consider the two simplest cases.

Case I: If we assume that points, once in contact, move with c until released, we have

$$\boldsymbol{v}^1 = \boldsymbol{v}^2 . \tag{6}$$

For this model we say that a no-slip, or perfect friction, condition is achieved on c. Eqs. (4) and (6) and condition (5) characterize the interface conditions for this case.

Case II: We may create the interface conditions for a frictionless, sliding contact by asserting that the tangential part of each $\boldsymbol{t}^\alpha$ is identically zero:

$$\boldsymbol{t}^\alpha - (\boldsymbol{t}^\alpha \cdot \boldsymbol{n}^\alpha)\boldsymbol{n}^\alpha = \boldsymbol{o} . \tag{7}$$

Eq. (7) along with (3)–(5) are the interface conditions for this case.

3. The class of Hertzian problems

We call problems "Hertzian" if the contact surface is approximately planar and the bodies have undergone small straining in the neighborhood of the contact surface. Specifically, we make the following assumptions:

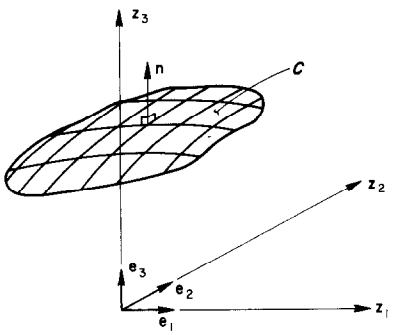

Fig. 2. Contact surface for Hertzian problems.

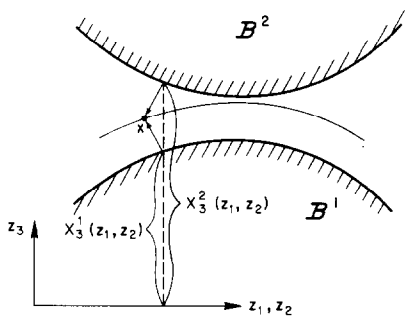

Fig. 3. Configuration of bodies and alignment of points which eventually contact in Hertzian problems.

(i) The unit normal vector with respect to the contact surface c is $\boldsymbol{n} \equiv n_i \boldsymbol{e}_i \approx \boldsymbol{e}_3$, where the n_i indicate components with respect to the standard basis $\{\boldsymbol{e}_i\}_1^3$ for R^3, (see fig. 2).

(ii) The ratio of area elements on the contact surface between the deformed and undeformed bodies differs negligibly from unity. Thus the Cauchy and Piola-Kirchhoff traction vectors for body number α ($\boldsymbol{t}^\alpha$ and $\boldsymbol{T}^\alpha$, respectively) are approximately equal, i.e., $\boldsymbol{t}^\alpha \approx \boldsymbol{T}^\alpha$.

Assumptions (i) and (ii) together imply that

$$t_3^\alpha \approx \boldsymbol{t}^\alpha \cdot \boldsymbol{n} \approx \boldsymbol{T}^\alpha \cdot \boldsymbol{n} \approx T_3^\alpha ,$$

$$\{t_1^\alpha, t_2^\alpha, 0\} \approx \boldsymbol{t}^\alpha - (\boldsymbol{t}^\alpha \cdot \boldsymbol{n})\boldsymbol{n} \approx \boldsymbol{T}^\alpha - (\boldsymbol{T}^\alpha \cdot \boldsymbol{n})\boldsymbol{n} \approx \{T_1^\alpha, T_2^\alpha, 0\} .$$

(iii) Material points which eventually contact have, to the first order, the same initial coordinates z_1, z_2. This is depicted in fig. 3.

We emphasize that the realm of applicability of our formulation involving the above assumptions is considerably greater than that to which Hertz's classical theory applies.

4. Spatial discretization of the bodies and contact surface

The methods we use to discretize problems into finite element models are standard (see e.g. [4]) except for our simulation of the contact surface which we shall now describe.

Let us assume for the moment that two bodies are in contact along the surface c. If we add a term of the form

$$\int_c \boldsymbol{\tau} \cdot (\boldsymbol{x}^1 - \boldsymbol{x}^2)\, \mathrm{d}c , \tag{8}$$

to a standard variational formulation for two independent bodies (see [5] for further details), then the enforcement of compatibility along the surface c will be achieved by way of taking independent variations of $\boldsymbol{\tau}$ (x^α are the deformed coordinates of material points in body α, and $\boldsymbol{\tau}$ is interpreted as the Cauchy traction vector across the contact surface). We note that, by assumption (i) above, c may be replaced in (8) by its projection upon the z_1-z_2 plane.

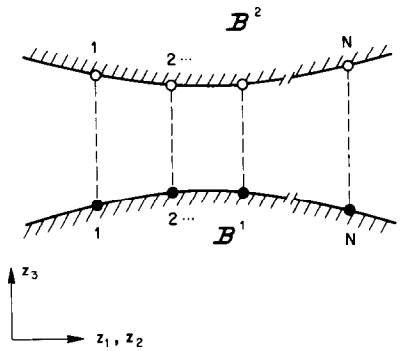

Fig. 4. Schematic of initial configuration of bodies and alignment of candidate contact nodes for the Hertzian case.

Our finite element discretization of (8) is achieved by availing ourselves of the particularly simple nature of (8), i.e. there are no derivatives of τ or x^α. Thus we may assume that τ consists of Dirac delta functions located at nodal points, as long as the finite element displacement functions are continuous at the nodes, which is assured. Thus (8) becomes in this case

$$\sum_{i=1}^{3}\sum_{j=1}^{N} \tau_{ij}(x_{ij}^1 - x_{ij}^2)\,, \tag{9}$$

where $i = 1, 2, 3$ refers to the spatial direction of components and N is the total number of pairs of nodes designated as candidates for contact (see fig. 4). The τ_{ij} are interpreted as nodal contact forces.

Eqs. (8) and (9) apply when there are tangential as well as normal contact forces. To achieve a frictionless condition on the contact surface, we simply delete the $i = 1, 2$ terms in (8) and (9); namely

$$\int_c \tau\,(x^1 - x^2)\,\mathrm{d}c\,, \tag{10a}$$

$$\sum_{j=1}^{N} \tau_j\,(x_j^1 - x_j^2)\,, \tag{10b}$$

where for simplicity we have omitted the subscripts 3 on τ and x^α. Here τ_j is interpreted as the nodal contact force in the normal direction. To simplify our presentation we will henceforth only discuss the frictionless case (10).

In assembling our global matrix equations, we include the τ_j in our vector of unknowns along with the nodal displacement components. Thus we like to think of (10b) as giving rise to a *contact element stiffness matrix*, which for the jth contact point is

$$\begin{bmatrix} 0 & 1 & 0 \\ 1 & 0 & -1 \\ 0 & -1 & 0 \end{bmatrix} \begin{bmatrix} x_j^1 \\ \tau_j \\ x_j^2 \end{bmatrix} \tag{11}$$

When the nodes corresponding to the jth contact point are in contact we add (11) to the global stiffness matrix. Otherwise we replace (11) by

$$\begin{bmatrix} 0 & 0 & 0 \\ 0 & 1 & 0 \\ 0 & 0 & 0 \end{bmatrix} \begin{bmatrix} x_j^1 \\ \tau_j \\ x_j^2 \end{bmatrix}, \tag{12}$$

which uncouples the two nodes corresponding to the jth contact point and results in $\tau_j = 0$.

The preceding description gives a rough idea of how the basic structure of the matrix equations is changed to account for Hertzian contact. More details concerning the actual steps of the incremental-iterative process are contained in section 7.

5. Contact problems involving bodies of different dimensions

The preceding formulation needs only trivial modification to be made applicable to contact problems involving bodies of different dimensions. There are many cases of considerable interest which fall into this category (e.g. solids contacting plates or shells). The modifications necessary are essentially interpretive. An example illustrates this assertion.

Consider the frictionless Hertzian contact of a three-dimensional solid and a two-dimensional plate. Let B^1 represent the solid and B^2 the plate. The contact term is exactly as before, i.e. (10). However, note that in this case c is also identifiable with part of the two-dimensional "volume" of the plate rather than its boundary. Thus τ contributes to the transverse momentum equation (or equilibrium equation in the case of statics) of the plate rather than to its boundary conditions. The interpretation of τ is thus two-fold, i.e. it is the normal component of the traction vector with respect to B^1, as before, and it is also the normal component of the "body force" with respect to B^2 (fig. 5).

This interpretation is general – namely, for one and two-dimensional bodies the contact force is an equivalent "body force" which contributes to the momentum equations rather than to the boundary conditions.

It should be noted that the contact element described in section 4 applies to the case of bodies of different dimension since the load on each body results from a term like (9) or (10).

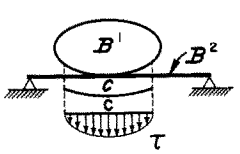

Fig. 5. Schematic of the contact of a solid and plate.

6. Temporal discretization

We use the Newmark method to temporally discretize the matrix equations of motion. This method amounts to a one-step integration formula involving two parameters which can be adjusted to control stability and numerical dissipation. Applications of the Newmark method to linear elastodynamic problems have been studied by many authors (e.g. see Goudreau–Taylor [6]). Briefly, the algorithm is given by

$$\boldsymbol{u}_{n+1} = \boldsymbol{u}_n + \Delta t\, \dot{\boldsymbol{u}}_n + (1/2 - \beta)\, \Delta t^2 \ddot{\boldsymbol{u}}_n + \beta \Delta^2 \ddot{\boldsymbol{u}}_{n+1} , \tag{13a}$$

$$\dot{\boldsymbol{u}}_{n+1} = \dot{\boldsymbol{u}}_n + (1 - \gamma)\, \Delta t\, \ddot{\boldsymbol{u}}_n + \gamma \Delta t \ddot{\boldsymbol{u}}_{n+1} , \tag{13b}$$

where $\boldsymbol{u}_n = \boldsymbol{u}(t_n)$ is the displacement vector at time t_n, $\Delta t = t_{n+1} - t_n$, β and γ are the two parameters, and a superposed dot indicates time differentiation. For linear elastic problems $\gamma = 1/2$ produces no dissipation, and $\beta \geqslant 1/4$ produces unconditional stability.

If the mass matrix $\boldsymbol{M}$ is diagonal (lumped mass), $\beta = 0$, and the stiffness matrix $\boldsymbol{K}$ and load vector $\boldsymbol{R}$ are independent of $\dot{\boldsymbol{u}}$, then the method is explicit, i.e. the solution can be advanced without solving a large set of simultaneous equations at each time step. Otherwise the method is implicit and equations must be solved.

7. Discrete impact and release conditions

The static aspects of the Hertzian algorithm (cf. section 4) are relatively simple. However, the dynamic aspects, especially the impact and release conditions, are quite delicate. To motivate this aspect of our work, consider the following hypothetical situation.

Assume that we are in the process of numerically solving some impact problem and suppose that it is discovered as we monitor the motion of the bodies that they impact somewhere in the time interval (t_1, t_2). At time t_1 we know the states of both bodies and we know that somewhere between t_1 and t_2 they have coalesced over a portion of their boundaries. Assume for the moment we know the geometry of the contact surface c. The question which arises then is what is the state of c at time t_2, i.e. what are the tractions, velocities and accelerations on c? It is necessary to know this information to carry forth the step-forward time integration. The appropriate values can be deduced from a local, wave-propagation analysis involving the theory of propagating singularity surfaces (see [5] section 7 for further details). A similar situation occurs when the bodies dynamically release.

In the remainder of this section we shall present the discretized impact and release conditions for the case of linearly elastic bodies. Throughout, we employ a lumped, rather than consistent, mass matrix. This renders the presentation more concise and leads to significant computational simplifications. For the low-order elements (e.g. bilinear) that we use in our analyses this represents no loss in accuracy.

For simplicity, we shall consider the frictionless case and isolate one pair of candidate contact nodes. The equations of motion for these nodes will be denoted

$$M^\alpha \ddot{u}^\alpha + K^\alpha(u^\alpha) - (-1)^\alpha \tau = 0 , \tag{14}$$

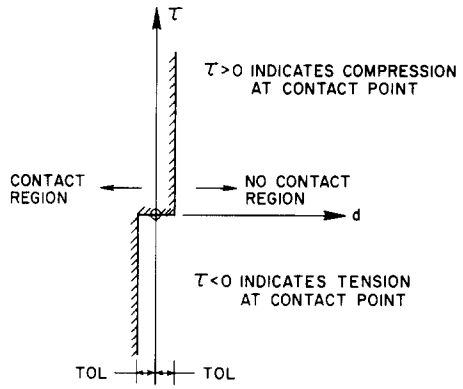

Fig. 6. Contact logic.

where the superscripts indicate the body number, M^α is the lumped mass coefficient, $K^\alpha(u^\alpha)$ is the elastic force and τ is the nodal contact force. If the bodies are not in contact $\tau = 0$; otherwise $\tau > 0$.

Let us suppose that at the end of the previous time step these candidate nodes were not in contact. Furthermore, assume that in the process of computing the present state, contact has been made. This occurs whenever

$$\text{(i) } d \equiv x^1 - x^2 < -TOL \quad \text{or} \quad \text{(ii) } d < TOL \text{ and } \tau > 0\,, \tag{15}$$

where TOL is a small positive number which acts as a safeguard against round-off. (In our finite element analysis program FEAP, we are currently using $TOL = 10^{-10}\,L$, where L is a problem dependent characteristic length.) This logic is displayed graphically in fig. 6. As a result of coming into contact, the algorithm makes the displacements compatible, i.e. $u^2 - u^1 = d_0 \equiv X^1 - X^2$, where X^1, X^2 are the coordinates of the particles in the initial configuration. However, the velocities $\dot{u}^1$, $\dot{u}^2$ and accelerations $\ddot{u}^1$, $\ddot{u}^2$ are left as computed by the algorithm. It is at this point that we impose the impact conditions. We denote by V_+, τ_+ and $\ddot{u}_+$ the corrected values of velocity, contact force and acceleration assigned to the pair of nodes in contact. They are given as follows:

$$V_+ = \frac{(\rho_0^2 U^2 \dot{u}^2_{-1} - \rho_0^1 U^1 \dot{u}^1_{-1})}{(\rho_0^2 U^2 - \rho_0^1 U^1)}\,, \tag{16a}$$

$$\tau_+ = \tau_- - \frac{M^1 M^2}{(M^1 + M^2)} (\ddot{u}^2_- - \ddot{u}^1_-)\,, \tag{16b}$$

$$\ddot{u}_+ = \frac{(M^1 \ddot{u}^1_- + M^2 \ddot{u}^2_-)}{(M^1 + M^2)}\,, \tag{16c}$$

where ρ_0^α is the density of body α in the initial configuration, U^α is an appropriate wave velocity for body α (e.g. U^α is dilatational velocity for three-dimensional linear elastic bodies, whereas it is "bar-wave" velocity in simple bar theory), the subscript (-1) refers to values taken at the end of the previous time step, and the subscript $(-)$ indicates values taken at the end of the last iteration of the present time step. Note that the right-hand side of (16a) depends on data computed prior to impact (i.e. $\dot{u}^1_{-1}$, $\dot{u}^2_{-1}$). This is consistent with wave-propagation theory and is important in numerical computations. For example, using data from the last iteration of the present time step (i.e. $\dot{u}^1_-$, $\dot{u}^2_-$) leads to markedly inferior numerical results (e.g. spike overshoots and oscillations about the correct values). On the other hand, τ_+ and $\ddot{u}_+$ are computed from data obtained in the last iteration (i.e. τ_-, $\ddot{u}^1_-$, $\ddot{u}^2_-$). The argument for this goes as follows. In the post-impact state there should be a unique value of τ_+ and $\ddot{u}_+$ assigned to the contact point. Since the values of u^1_- and u^2_- are already compatible, we employ (14) to solve for τ_+ and $\ddot{u}_+$. That is we set

$$M^\alpha \ddot{u}_+ + K^\alpha(\boldsymbol{u}^\alpha_-) - (-1)^\alpha \tau_+ = 0 \tag{17}$$

and substract (17) from (14) evaluated at the previous iteration:

$$M^\alpha \ddot{u}^\alpha_- + K^\alpha(\boldsymbol{u}^\alpha_-) - (-1)^\alpha \tau_- = 0\,. \tag{18}$$

This is how we arrive at (16b, c). Satisfaction of the equations of motion is automatically achieved for the post-impact state as a result of (17).

Now we shall describe the release conditions. These stem from the same concepts as the impact conditions. In fact, one way to look at the release conditions is to view them as impact conditions with time running backwards. Thus from a local wave-propagation analysis we obtain the post-release velocities V^1_+ and V^2_+ from the pre-release data τ_{-1} and V_{-1} as follows:

$$V^\alpha_+ = V_{-1} + (-1)^\alpha \tau_{-1}/\rho_0^\alpha U^\alpha A^\alpha\,, \tag{19}$$

where A^1, A^2 are tributary area weighting factors for the respective candidate nodes. Simultaneously we need τ_+ to be equal to zero. We set $\tau_+ = 0$ and adjust the accelerations in (14) so that this change maintains satisfaction of the equations of motion. The computation is analogous to the one in which we calculated (16b, c):

$$\ddot{u}^\alpha_+ = \ddot{u}^\alpha_- - (-1)^\alpha \tau_-/M^\alpha\,, \tag{20}$$

where here $\ddot{u}^1_+$ and $\ddot{u}^2_+$ are the corrected post-release accelerations, and $\ddot{u}^1_-$, $\ddot{u}^2_-$ and τ_- are the values computed from the last iteration of the present time step.

We determine whether or not release has occurred in the following way. If $\tau < 0$ (tension across the contact surface in any iteration) we release; if $\tau > 0$, but less than 2% of the previous time step value τ_{-1}, we also release. Otherwise we retain contact. The last release case above was arrived at from numerical experimentation. For example, problems were run for releasing bars in which the theoretical drop-off of τ was 100% in one time-step (shock waves). Our numerical computations predicted this drop-off quite accurately producing a positive τ of less than 10^{-3} times the previous value. Interpreting this as contact, the algorithm did not release the bars until the next time step,

at which time the update indicated in (19) and (20) had negligible effect due to the very small value of τ_-. We deduced the criterion above from cases like this.

The only pitfall in using this criterion can be seen as follows. Suppose the actual drop-off during a time step in a problem is greater than 98% of the previous value, but the exact solution from this point on is constant at some small positive τ. The algorithm would release and not join the nodes until the next time step. From here on everything would run as it should.

Under appropriate circumstances, the formulas

$$V_+ = \frac{(M^2 \dot{u}^2_{-1} + M^1 \dot{u}^1_{-1})}{(M^1 + M^2)}, \tag{21a}$$

and

$$V^\alpha_+ = V_{-1} + (-1)^\alpha \Delta t \, \tau_{-1} / 2M^\alpha , \tag{21b}$$

may be used in place of (16a) and (19), respectively; one needs that the mesh is regular in the sense that $(\Delta X_3)^\alpha = \Delta t U^\alpha$, where $(\Delta X_3)^\alpha$ is the height of the element in body α (see fig. 7). Eq. (21b) has the desirable property of eliminating the need of computing the area weighting factors in (19). These ideas, as well as more refined methods of computing discrete impact and release conditions, will be dealt with in future work of the authors.

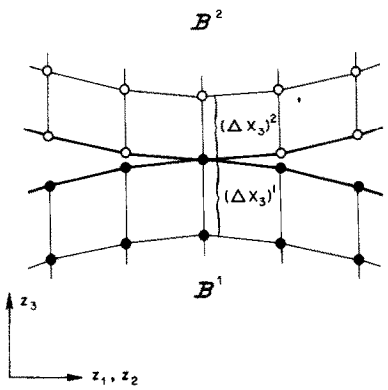

Fig. 7. Schematic of finite element meshing in neighborhood of contact region.

8. Solution of the nonlinear algebraic problem

In this section we shall assume that all contact force degrees of freedom are included in the nodal "displacement" vector $\boldsymbol{u}$. For simplicity we shall also only deal with the nonlinear elastic case.

Let the equations of motion for both bodies and the contact forces be written

$$\boldsymbol{M}\ddot{\boldsymbol{u}} + \boldsymbol{K}(\boldsymbol{u}) = \boldsymbol{R} , \tag{22}$$

where M is the mass matrix, $K(u)$ is the vector of elastic and contact forces and R is the external load vector. Assuming β and $\Delta t \neq 0$, use of the Newmark formula (13a) in (22) yields the nonlinear algebraic equation

$$\frac{1}{\beta \Delta t^2} M u_{n+1} + K(u_{n+1}) = R_{n+1} + M A_n , \tag{23}$$

where

$$A_n = \frac{1}{\beta}\left[\frac{1}{\Delta t^2} u_n + \frac{1}{\Delta t} \dot{u}_n + \left(\frac{1-2\beta}{2}\right) \ddot{u}_n\right].$$

We solve (23) via the following Newton–Raphson iterative procedure.

Let a superscript in parentheses indicate the iteration number. The 0 and $i+1$ iterative solutions at time t_{n+1} are then given by

$$u_{n+1}^{(0)} = u_n$$

and (24)

$$u_{n+1}^{(i+1)} = u_{n+1}^{(i)} + \Delta u_{n+1}^{(i)} ,$$

respectively, where $\Delta u_{n+1}^{(i)}$ satisfies the linear equation

$$K^* \Delta u_{n+1}^{(i)} = R^* , \tag{25}$$

where

$$K^* = \frac{1}{\beta \Delta t^2} M + DK(u_{n+1}^{(i)}) \quad \text{and} \quad R^* = R_{n+1} - K(u_{n+1}^{(i)}) + M\left(A_n - \frac{1}{\beta \Delta t^2} u_{n+1}^{(i)}\right),$$

in which DK indicates the tangent stiffness. Iteration continues until

$$\| \Delta u_{n+1}^{(i)} \| \leqslant \epsilon \| u_{n+1}^{(i)} \| , \tag{26}$$

where $\| \cdot \|$ is the Euclidean norm (i.e. $\| x \| = (\Sigma x_i^2)^{1/2}$), and ϵ, the error tolerance, is a preassigned "small" positive number of order Δt. A summary of the resulting algorithm is contained in table 1.

Static analysis may be carried out with this algorithm by formally setting $M = O$.

9. Sample problems

In sample problems 9.1 and 9.4–9.9, bilinear displacement elements are employed. In 9.2 and 9.3, standard linear displacement elements are employed.

Table 1. Summary of the contact-impact algorithm

1. Initialize K^* to zero, input Δt for the sequence.
2. For each time sequence in the analysis compute contribution to K^* for each continuum finite element.
3. Determine the first equation (say number N) in K^* which will be modified by the remaining contact elements.
4. Factor K^* to equation $N-1$ using Gauss elimination and place the factored K^* into backing storage.
5. For each step or iteration in the sequence read the partially factored K^* into core.
6. Initialize R^* to the current load level R.
7. For the continuum elements compute the contribution to R^*.
8. For the contact elements determine the state of penetration and add the appropriate contributions to K^* and R^*. This completes formation of K^*.
9. Reduce R^*, complete factoring of K^*, and back substitute to determine $\Delta u_{n+1}^{(i)}$.
10. Update solution $u_{n+1}^{(i)}$ and check for convergence. If convergence test is satisfied, continue; otherwise repeat steps 5 to 10.
11. Output solution displacements and stresses, compute new time, and complete update of displacements, velocities and accelerations.
12. For each time step in the sequence repeat steps 5 to 11.
13. For each sequence repeat steps 1 to 12.

9.1. Hertz contact problem

The Hertz static contact problem (see [7]) was solved, and we were able to accurately compute both the contact region and the pressures over a wide range of loading. The mesh is depicted in fig. 8, and contact pressure versus contact radius results are plotted in fig. 9. The data are:

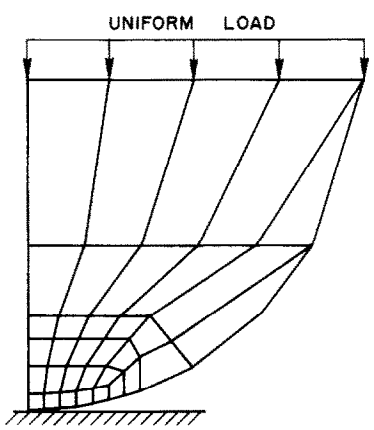

Fig. 8. Finite element mesh for Hertz static contact problem.

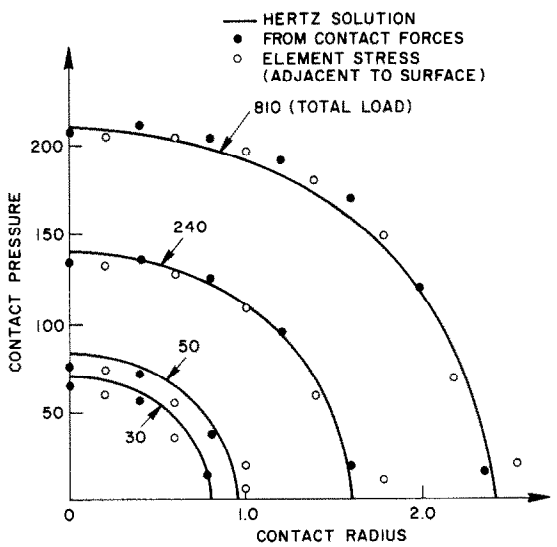

Fig. 9. Comparison of results of finite element solution and Hertz solution of static contact problem.

$E = 1000$ (Young's modulus),

$\nu = .3$ (Poisson's ratio),

$R = 8$ (radius of quarter sphere).

The total applied force is distributed uniformly across the top surface.

The nodal contact forces were converted to contact pressures by a tributary area method. The results clearly indicate that the contact pressures are given more accurately by the nodal contact forces than by the element stresses, as one might surmise they would be.

9.2. *Impact of two identical elastic bars*

This problem, although extremely simple to solve analytically, is a source of considerable insight as regards impact and release phenomena. Since the definition of the contact surface (a point) is trivial, we are able to focus in completely on the importance of achieving a theoretically correct impact and release. The data are given in fig. 10. The results (figs. 11–14) are tracings of computer plots which employ linear interpolation between time steps. The stress data (fig. 14) are to be viewed as occurring at the center of the element. Since the numerical results are so close to the exact ones we did not include the latter so as not to crowd the plots.

Newmark data for these runs consisted of $\beta = .001001$, $\gamma = .502$ up to time .2, and then $\beta = .001001$, $\gamma = .525625$ between .2 and .5. The reason for increasing γ (which increases the numerical dissipation) in the second time sequence was to mitigate the effects of an apparent instability. The original time sequence data are right at the stability limit. As the analysis proceeds, some noise becomes amplified at the boundaries. Some of this noise is visible in fig. 14.

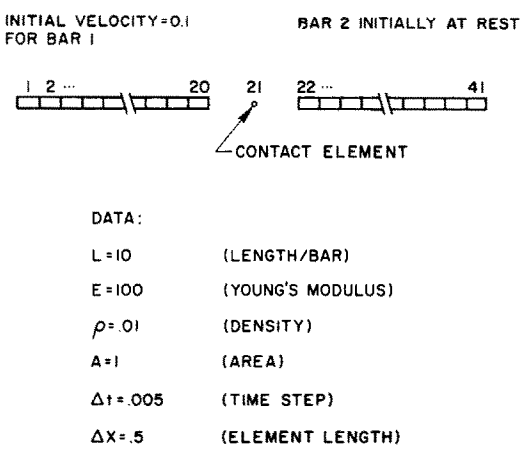

Fig. 10. Data for the impact of two identical bars.

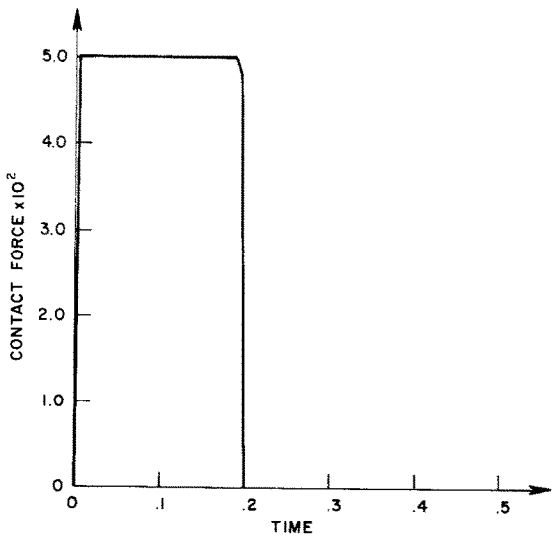

Fig. 11. Impact of two identical bars. Contact force vs. time.

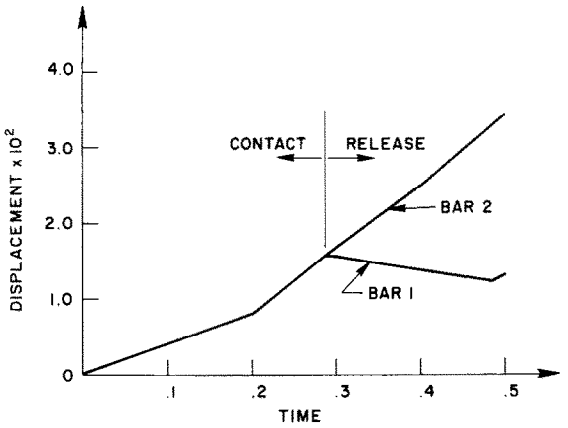

Fig. 12. Impact of two identical bars. Displacements of contact points vs. time.

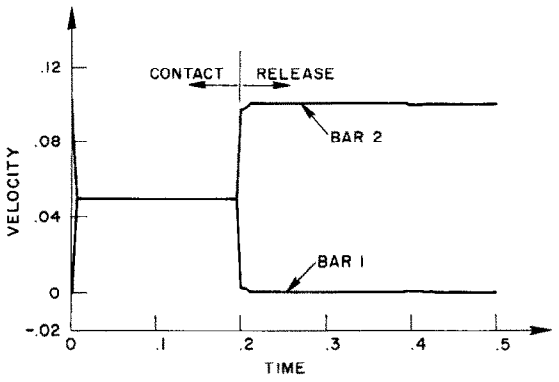

Fig. 13. Impact of two identical bars. Velocities of contact points vs. time.

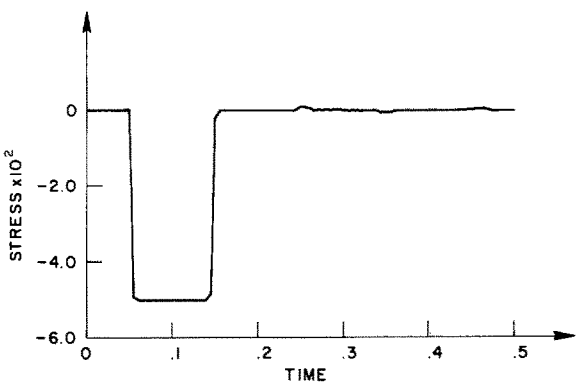

Fig. 14. Impact of two identical bars. Stress in element 32 vs. time.

The discontinuous stress and velocity waves which result after impact are difficult to capture numerically, especially with a coarse gird, as employed here. Our results, figs. 11–14, indicate the veracity and importance of the impact and release conditions. Note how effectively the impact conditions bring the contact force from zero to the exact value in one time step without any overshoot (fig. 11). The release (at $t = .2$) is also very crisp. The slight perturbation from the exact solution (fig. 13), which is due to the Newmark algorithm, could be made to go away completely with mesh refinement.

Lack of space prevents us from including some "negative" results obtained by not using the impact and release conditions discussed in section 7. These results possess spike overshoots around wave fronts, oscillations about the exact solution, and spurious release waves. As can be seen from figs. 11–14, they are entirely eliminated by imposing the impact and release conditions.

9.3. Impact of two dissimilar elastic bars

This problem is slightly more complicated than the previous problem. Here again the length of each bar is 10, and the initial conditions, density and area are the same as in fig. 10. However, we

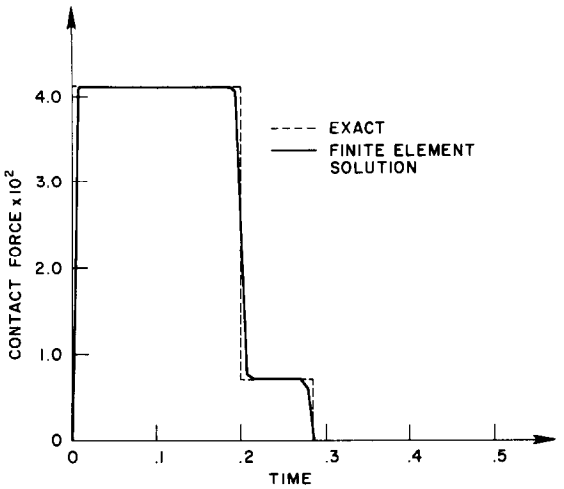

Fig. 15. Impact of two dissimilar bars. Contact force vs. time.

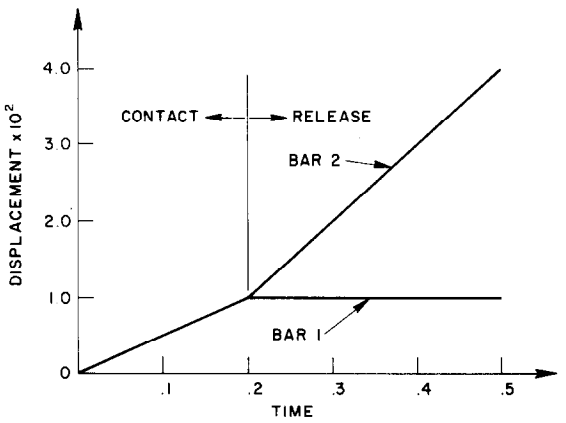

Fig. 16. Impact of two dissimilar bars. Displacements of contact points vs. time.

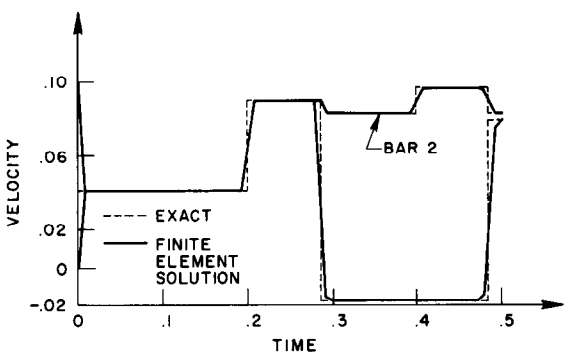

Fig. 17. Impact of two dissimilar bars. Velocities of contact points vs. time.

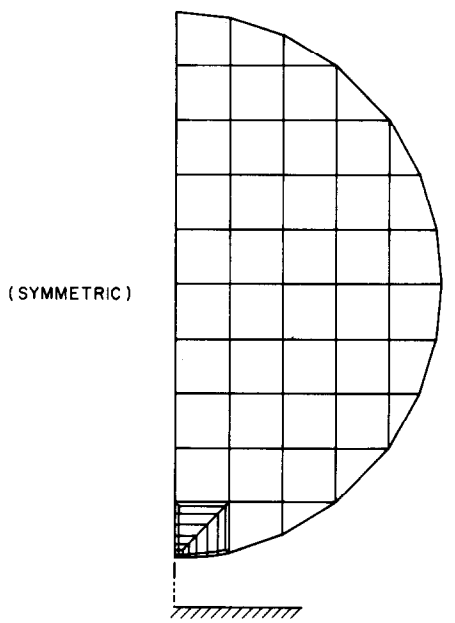

Fig. 18. Finite element mesh for impact of an elastic sphere against a rigid wall.

have taken the elastic moduli of the bars to be different, namely $E_1 = 49$ and $E_2 = 100$. Bar 1 is subdivided into 20 equal-length elements and bar 2 into 14. The time step $\Delta t = .00714$ and $\beta = .001001$, $\gamma = .502$. The results, depicted in figs. 15–17, are remarkably accurate.

9.4. Impact of an elastic sphere against a rigid surface

The mesh for this problem is depicted in fig. 18. The data are:

$\rho = .01$ (density),

$E = 1000$ (Young's modulus),

$\nu = .3$ (Poisson's ratio),

$R = 5$ (radius of sphere),

$\Delta t = .01$ (time step),

$\beta = .25, \quad \gamma = .5$ (Newmark parameters).

The sphere was subjected to an initial, uniform velocity of .3 (downward). The normal pressure distribution over the contact area at the time instant when the contact radius has spread to its maximum value compares favorably with the quasistatic approximate solution of Hertz [7] (see fig. 19).

In axisymmetric problems such as this one the contact element along the axis of symmetry should not be included. This is because of the basic assumption that the contact force consists of delta functions – this leads to no generalized force when the radius is zero. For demonstration purposes we have included it in this problem; it produces the spike in the nodal contact force data in fig. 19.

The effects of the initial impact were small in this problem, and large time steps did not markedly affect the results.

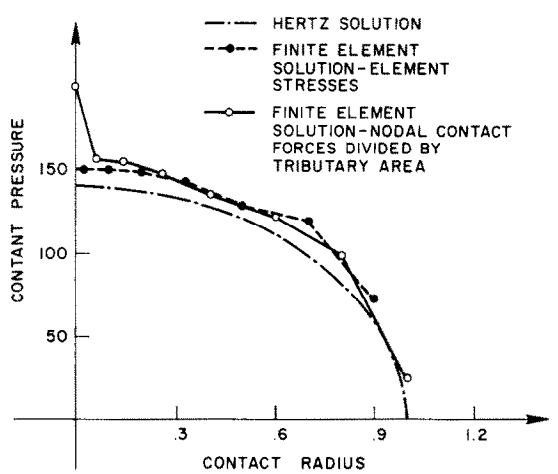

Fig. 19. Impact of an elastic sphere against a rigid wall. Contact pressure vs. contact radius at instant of maximum contact area development.

9.5. *Impact of two dissimilar elastic spheres*

The mesh for this problem is depicted in fig. 20. The data are:

$\rho_1 = .01$, $\rho_2 = .02$ (density),

$E_1 = 1000$, $E_2 = 2000$ (Young's modulus),

$\nu_1 = .4$, $\nu_2 = .2$ (Poisson's ratio),

$R_1 = 5$, $R_2 = 5$ (radius of sphere),

$\Delta t = .01$ (time step),

$\beta = .25$, $\gamma = .5$ (Newmark parameters).

The uniform initial velocities of the spheres are $V_1 = 4.0$ (upward) and $V_2 = 2.0$ (downward). The shape of the computed contact surface at the instant of maximum contact area development is compared with the approximate quasistatic Hertz solution in fig. 21.

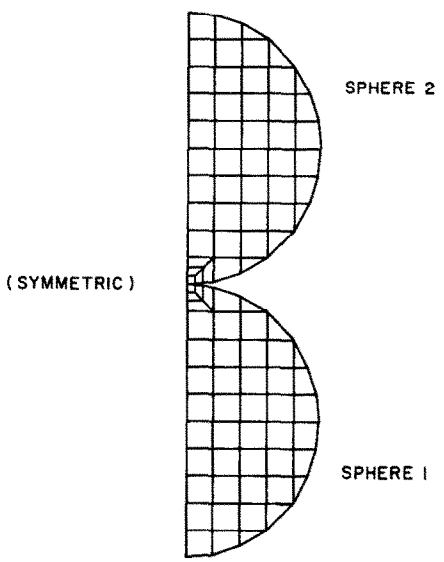

Fig. 20. Finite element mesh for impact of two dissimilar elastic spheres.

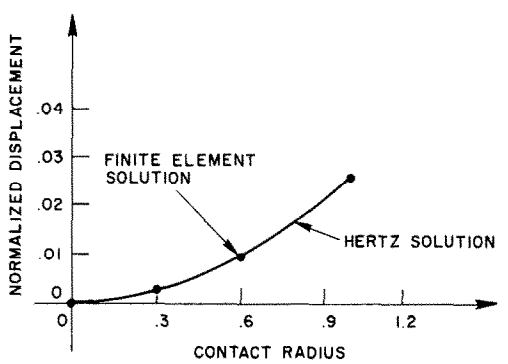

Fig. 21. Impact of two dissimilar elastic spheres. Shape of contact surface at instant of maximum contact area development.

9.6. *Head injury model*

Several contact-impact analyses of an axisymmetric spherical head model were performed (see [8]). The model consists of a three-layered skull and encapsulated brain (fig. 22). The radius of the

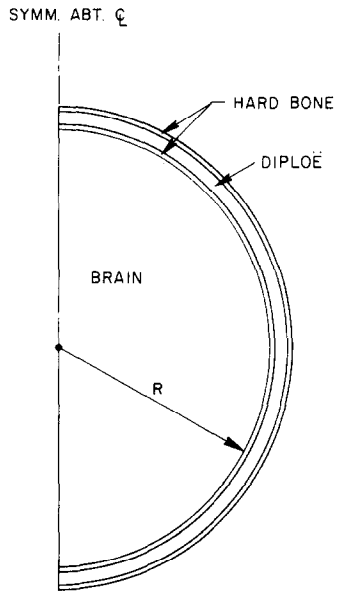

Fig. 22. Axisymmetric spherical head injury model.

brain cavity $R = 2.95$ in, the thickness of each hard bone layer is 0.05 in, and the thickness of the diploë is 0.10 in. Material properties are taken to be linear elastic and are given in table 2. In the skull, three layers of elements were used through the thickness and four-point Gaussian quadrature was employed. The brain elements make use of one-point quadrature.

(a) Hollow skull contacting a rigid surface

The skull was discretized into 51 elements and 7 candidate contact elements were employed (see fig. 23a). The skull is fixed at the uppermost node, and a rigid frictionless surface is pressed into it from the bottom. The rigid surface, initially just touching the skull, is given an upward motion of .1 in per step until a total motion of .5 in was achieved. Inertial effects were neglected.

Tracings of computer plotted deformed configurations and contact pressures (obtained from nodal contact forces by a tributary area method) are depicted in figs. 23b- 23f. Note how the peak contact pressure occurs towards the outer radius of the contact zone. This is a common

Table 2. Material properties for head injury model

Property	Hard bone	Diploë	Brain
K – bulk modulus (10^6 psi)	1.333	.1333	.305
G – shear modulus (10^6 psi)	.8	.08	.0305
ρ – density (10^{-4} lb-sec^2/in^4)	2	.2	.037

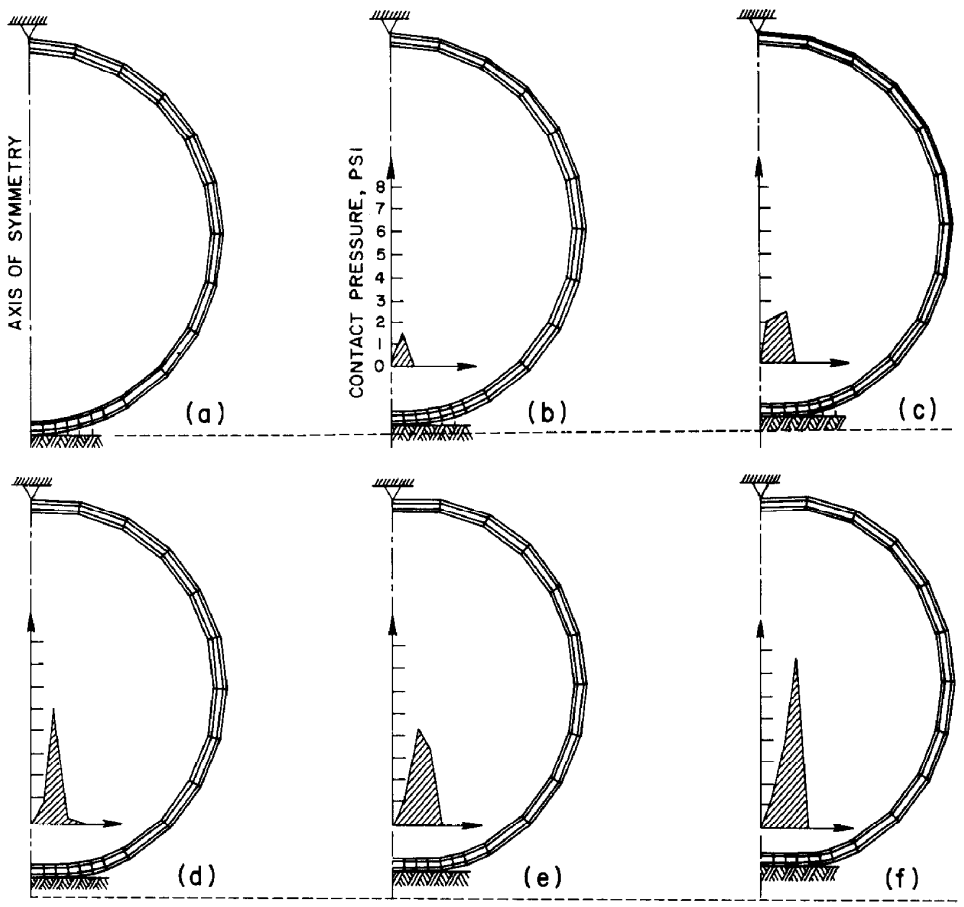

Fig. 23. Initial (a) and deformed (b–f) mesh configurations of a hollow skull model contacting a rigid surface.

feature of shell-like contact phenomena, but quite opposite that for a homogeneous elastic sphere (cf. fig. 9).

(b) Hollow skull impacting a rigid surface

The mesh of the previous problem is also used here. The data are:

$\Delta t = .05 \times 10^{-5}$ sec (time step)

$\beta = .25, \quad \gamma = .5$ (Newmark parameters).

The uniform initial velocity of the sphere was 352 in/sec (=20 mph) downward. In this example we were interested in seeing the early-time wave-propagation effects, and thus we employed a time step which is close to the transit time for a dilatational wave to travel through the thickness of each skull layer (the transit time for the hard bone layer equals $.0456 \times 10^{-5}$ sec). The contact force for the first 100 time steps is presented in fig. 24. The period of oscillation superposed

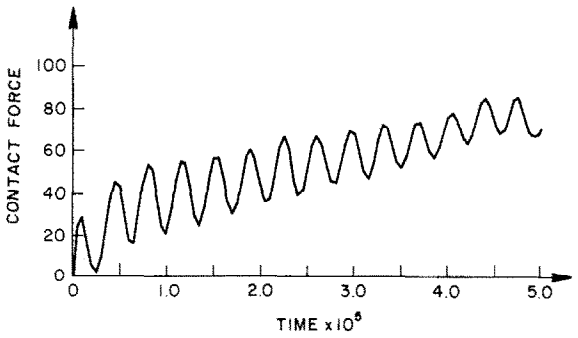

Fig. 24. Contact force vs. time for a hollow skull impacting a rigid surface.

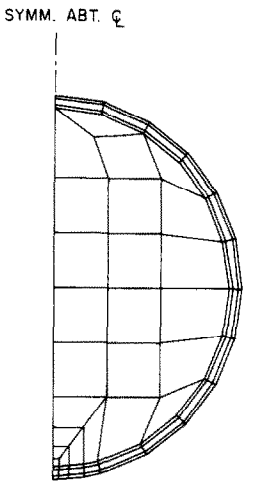

Fig. 25. Finite element mesh for impact of skull-brain model against a rigid surface.

upon the results is approximately $.35 \times 10^{-5}$ sec, which is very close to the time required for a dilatational wave to pass through the entire thickness of the skull and back (i.e. approximately $.365 \times 10^{-5}$ sec).

(c) Impact of skull-brain model against a rigid surface

The mesh for this problem is depicted in fig. 25. The modeling of the skull portion is identical to the previous two cases. Here we used a time step of $.365 \times 10^{-5}$ sec; all other data are the same as for the previous case. Pressure profiles over the contact surface, obtained from the nodal contact forces by a tributary area method, are depicted in fig. 26. It is interesting to compare these results

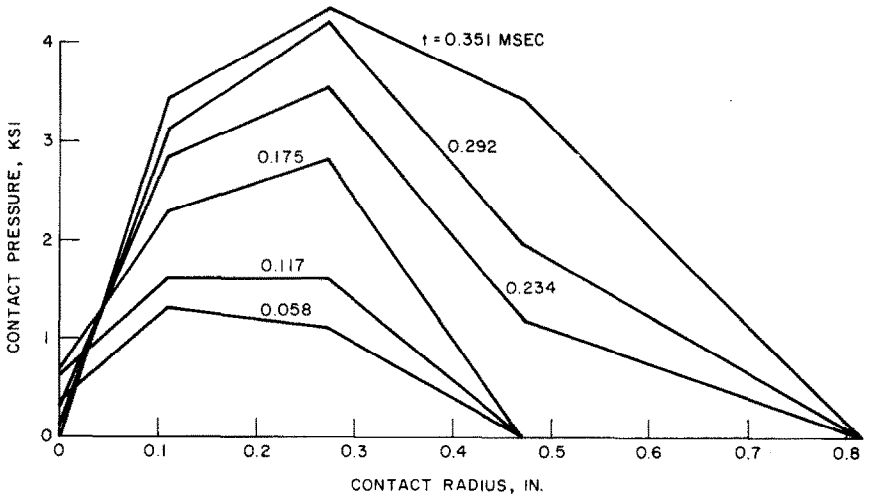

Fig. 26. Contact pressure profiles for skull-brain impact problem.

with the profiles obtained from the dynamic Hertz problem and the quasistatic shell problem, case (a). In the former case the peak contact pressure is located on the axis of symmetry (cf. fig. 19), and in the latter case it is towards the periphery of the contact zone, falling off to zero along the asymmetry axis (cf. fig. 23). Here in fig. 26 results somewhere in-between these extremes is achieved.

9.7. *Rectangular block impacting a rigid surface*

An analysis was performed of a plane strain linear elastic rectangular block impacting a rigid surface. The finite element mesh is shown in fig. 27. The data are:

$\rho = 0.1$ (density),

$E = 1000$ (Young's modulus),

$\nu = .3$ (Poisson's ratio),

$L = 9$ (length),

$\Delta t = .002725$ (time step),

$\beta = .001001, \quad \gamma = .502$ (Newmark parameters).

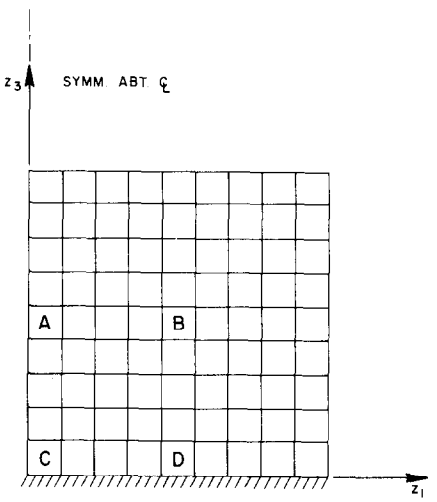

Fig. 27. Finite element mesh for a plane strain rectangular block impacting a rigid surface.

The time step is the transit time for a dilatational wave to propagate the length of one element. Initially the block is traveling at a uniform velocity of 1 (downward). The block impacts the rigid surface at $t = 0$. Outside the shaded zone (see fig. 28) defined by $R = ct$, where $c = 366.9$ is the dilatational wave velocity, the exact solution consists of two constant zones, I and II, separated

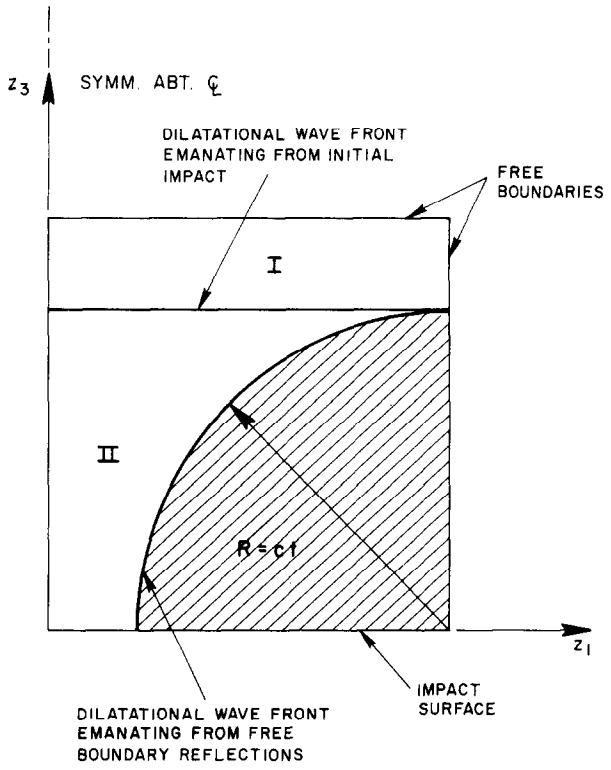

Fig. 28. Wave front diagram for rectangular block impact problem.

by the dilatational wave front which emanates from the initial impact. The circular wave front is a result of reflections off the right-hand side (free) boundary.

We were interested in determining the early time results for this problem which can be compared with the known solution in zone II and provide a test of the discrete impact conditions.

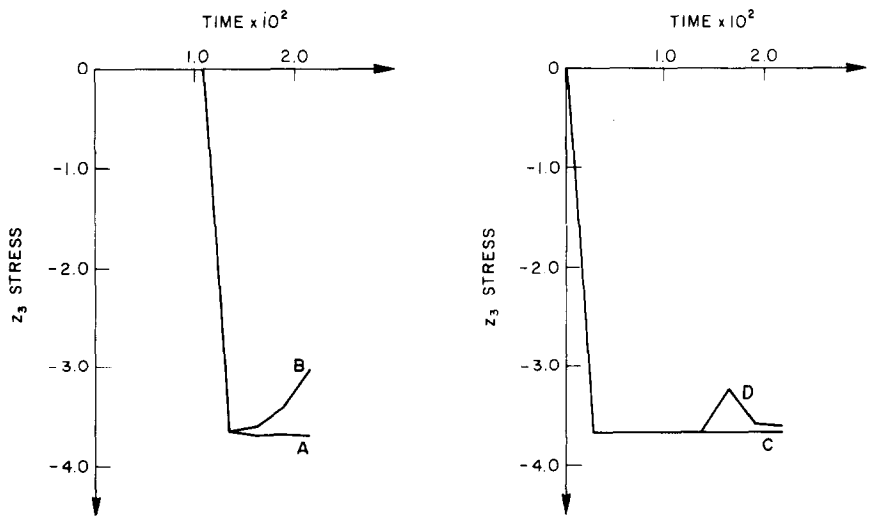

Fig. 29. Stress results for rectangular block impact problem.

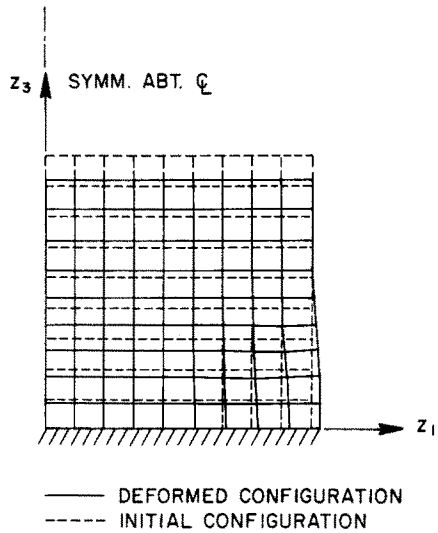

Fig. 30. Deformed configuration superposed upon initial configuration for rectangular block impact problem at time .0163. The displacements are magnified 50 times.

Eight time steps were run, allowing the front separating zones I and II to propagate to within one element length of the top surface. Stress results for several elements are depicted in fig. 29. In each case the rise of stress from zero to the exact value is achieved in one time step, and this value is maintained until the wave from the right-hand boundary reaches the element. The results corroborate the effectiveness of the discrete impact conditions.

A deformed mesh at $t = .0163$ with displacements magnified by a factor of 50 is superposed upon the undeformed mesh in fig. 30. At this time the plane front has traveled upward through 6 elements. Note that bulging along the right-hand side occurs up to this point. The effect of a frictionless contact surface is evidenced by the displacement to the right of the lower right-hand corner node.

9.8. Dynamic rigid punch problems

(a) Triangular punch

A rigid triangular punch is driven into a linear elastic half-plane at constant velocity $V = 100$. (see fig. 31). The data are:

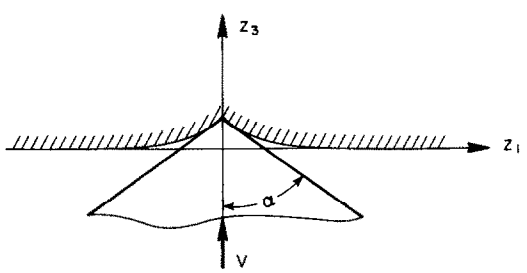

Fig. 31. Rigid triangular punch driven into a half-plane at constant velocity V.

ρ = .01 (density),

E = 1000 (Young's modulus),

ν = .3 (Poisson's ratio),

α = $\tan^{-1} 2$ (punch angle),

Δt = .0025 (time step),

β = .25, γ = .5 (Newmark parameters).

Five contact elements were employed. The initial mesh configuration and several deformed configurations are illustrated in fig. 32.

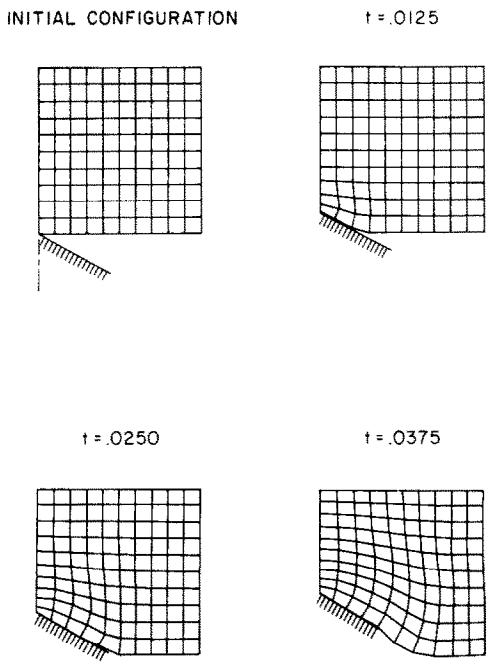

Fig. 32. Initial and deformed configurations for rigid triangular punch problem.

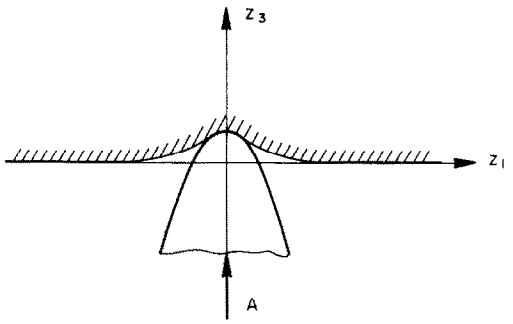

Fig. 33. Rigid parabolic punch driven into a half-plane at constant acceleration A.

(b) Parabolic punch

A rigid parabolic punch was driven into the half-plane at a constant acceleration A = 4000 (see fig. 33). The surface of the punch is defined by the equation $z_3 = (z_1)^2/8$. The remaining data are the same as in the previous case. The initial mesh configuration and deformed configurations are depicted in fig. 34.

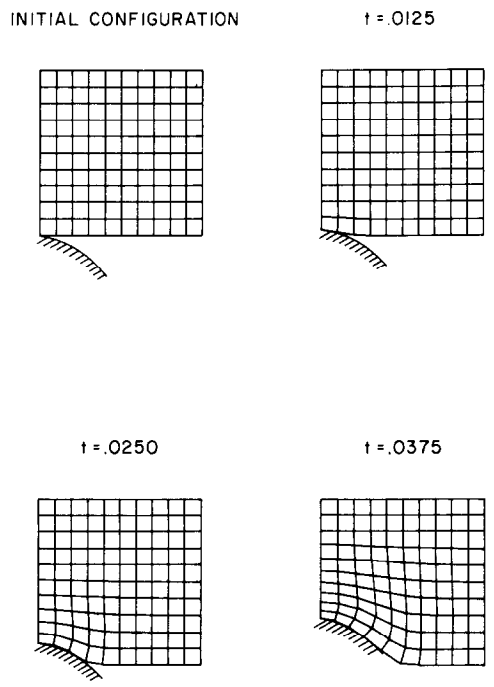

Fig. 34. Initial and deformed configurations for rigid parabolic punch problem.

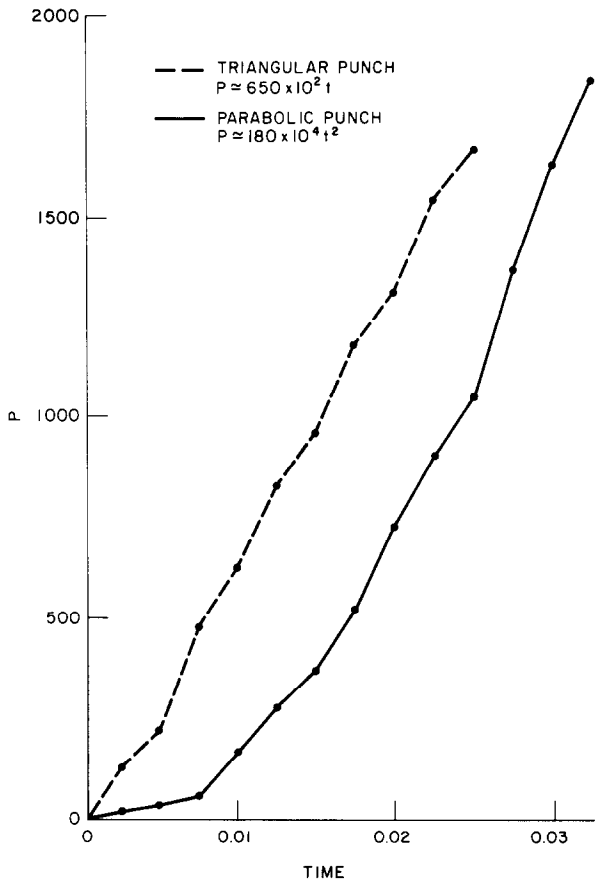

Fig. 35. Total contact force vs. time for rigid punch problems.

Total contact force for case (a) or (b) is known [9] to vary linearly or quadratically, respectively, with time. The results of the finite element analyses are seen to exhibit this behavior (see fig. 35).

The results for case (b) employed a modification to the velocity impact conditions. Specifically, the velocities of the last time step prior to impact, $\dot{u}^{\alpha}_{-1}$, in eq. (16a), were replaced by the velocities of the last iteration prior to impact, $\dot{u}^{\alpha}_{-}$. This was done because the impactor was accelerating, causing the velocities to vary linearly over the time step. Results using (16a), although showing the general trend of fig. 35, oscillated quite a bit before settling down. In general this artifice is *not* to be recommended; the sharp impact results of previous problems (namely the bar problems 9.2 and 9.3 and the block problem 9.7) would not have been obtained if this was made the rule rather than the exception. What this problem does emphasize is that more sensitive (i.e. higher-order) impact and release conditions are necessary if one is to avoid taking excessively small time steps during the impact and release phases of a contact problem.

9.9. Static analyses of germanium crystals

We have recently aided a research team of Berkeley physicists studying electron-hole drops in germanium (see for example [10]) by performing contact analyses of germanium crystals. Their work has been featured in lengthy articles in the San Francisco Chronicle, May 19, 1975, New York Times, May 19, 1975, and other major periodicals. Briefly, their theory indicates that long-lived electron-hole drops will occur around the point of maximum $\epsilon_{11} - \epsilon_{33}$, where ϵ_{ij} are the infinitesimal strains in stressed germanium crystals. Their experimental technique enables them to photograph the electron-hole drop (see fig. 36). This was the first direct photographic evidence of the existence of this phenomenon.

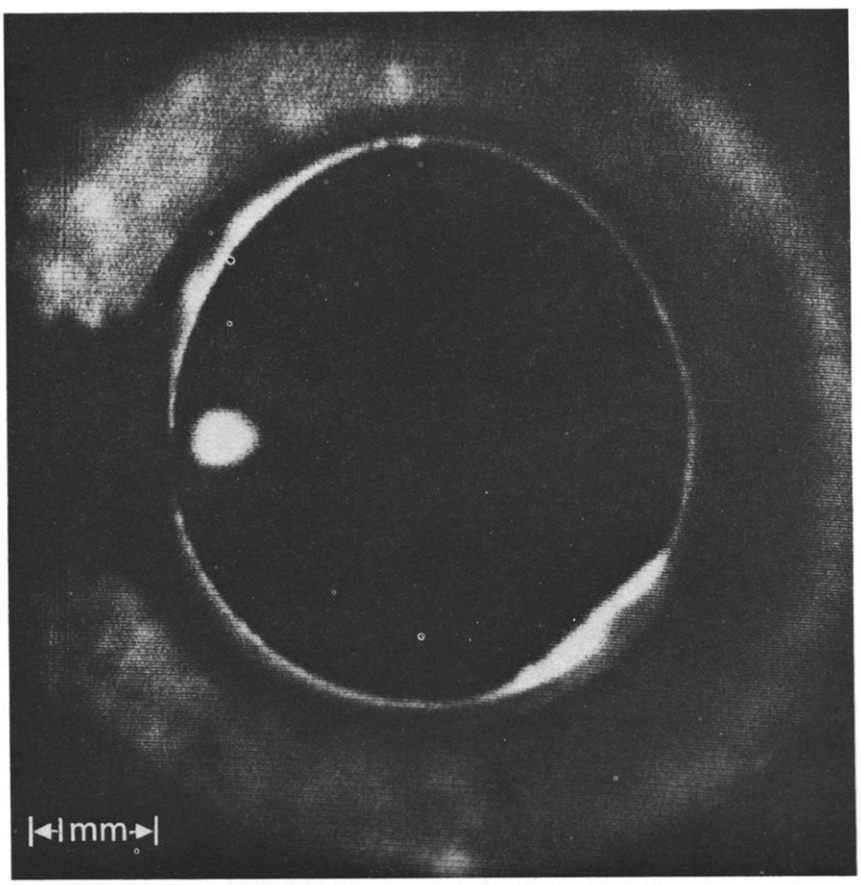

Fig. 36. First photograph of an electron-hole drop in germanium.

The Hertzian contact algorithm was employed to calculate the strain contours of sample crystals. For example, the following data were employed to analyze the plane strain configuration illustrated in fig. 37.

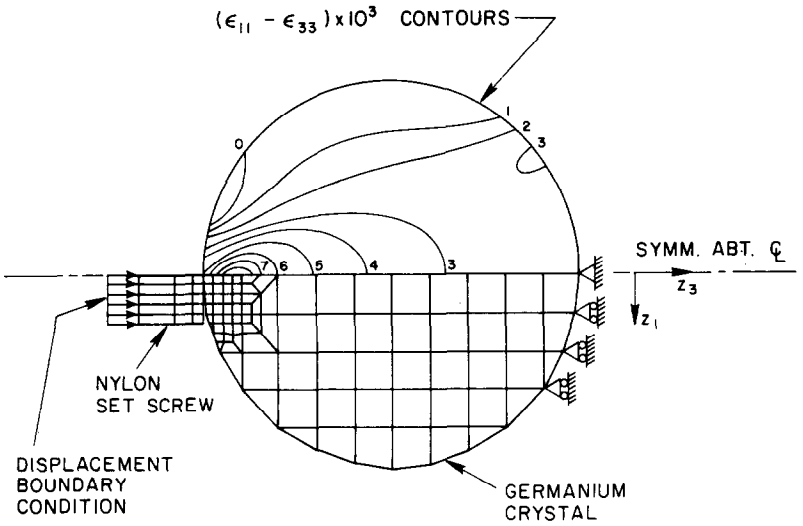

Fig. 37. Finite element mesh and strain contours for contact analysis of a germanium crystal.

Nylon set screw: $E = 1000$ dyn/cm^2 ,

$\nu = .3$,

Germanium crystal: $E = 13850$ dyn/cm^2 ,

$\nu = .3$.

The radius of the germanium crystal is 2 mm. The nylon set screw was driven into the crystal .08 mm, as illustrated in fig. 37, and five of the candidate contact nodes engaged. In fig. 37 we also show contours of $\epsilon_{11} - \epsilon_{33}$. The computed point of maximum $\epsilon_{11} - \epsilon_{33}$ is in close agreement with the photographed location of the electron-hole drop (cf. fig. 36).

Acknowledgement

The authors would like to thank T. Shugar and M. Katona, project monitors, of the Civil Engineering Laboratory, Naval Construction Battalion Center, Port Hueneme, California, for their continued support and interest; L. Ovenshire of the National Highway Traffic Safety Administration of the Department of Transportation for suggesting, and providing support for, the work reported upon herein; and K. Saczalski of the Office of Naval Research.

References

[1] A. Francavilla and O.C. Zienkiewicz, A note on numerical computation of elastic contact problems. To be published.

[2] T.F. Conry and A. Seireg, A mathematical programming method for design of elastic bodies in contact, J. Appl. Mech. 38 (1971) 387–392.
[3] S.H. Chan and I.S. Tuba, A finite element method for contact problems of solid bodies, Int. J. Mech. Sci. 13 (1971) 615–639.
[4] O.C. Zienkiewicz, The finite element method in engineering science (McGraw-Hill, New York, 1971).
[5] T.J.R. Hughes, R.L. Taylor and J.L. Sackman, Finite element formulation and solution of contact-impact problems in continuum mechanics, SESM Report No. 74-8 (Univ. California, Berkeley, May 1974). [Copies can be obtained from National Technical Information Service, Springfield, Virginia 22151, Accession No. PB-233 888/AS.]
[6] G.L. Goudreau and R.L. Taylor, Evaluation of numerical integration methods in elastodynamics, Comp. Meths. Appl. Mech. Eng. 2 (1972) 67–97.
[7] W. Goldsmith, Impact (Edward Arnold, London, 1960).
[8] T.A. Shugar and M.G. Katona, Development of Finite Element Head Injury Model, J. Eng. Mechs. Div. ASCE 101 (1975) 223–239.
[9] G.P. Cheupanov and E.F. Afanas'ev, Some dynamic problems of the theory of elasticity – a review, Int. J. Eng. Sci. 12 (1974) 665–690.
[10] J.P. Wolfe, W.L. Hansen, E.E. Haller, R.S. Markiewicz, C. Kittel and C.D. Jeffries, Photograph of an electron-hole drop in germanium, Phys. Rev. Letters 34 (1974) 1292–1293.